

FOCUS on Contamination: Hydrology-Informed Noise-Aware Learning for Geospatial PFAS Mapping

Jowaria Khan
University of Michigan
Ann Arbor, Michigan, USA
jowaria@umich.edu

Alexa Friedman
Environmental Working Group
Washington, DC, USA
alexa.friedman@ewg.org

Sydney Evans
Environmental Working Group
Washington, DC, USA
sydney.evans@ewg.org

Rachel Klein
University of Michigan
Ann Arbor, Michigan, USA
raklein@umich.edu

Runzi Wang
University of California, Davis
Davis, California, USA
mrrwang@ucdavis.edu

Katherine E. Manz
University of Michigan
Ann Arbor, Michigan, USA
katmanz@umich.edu

Kaley Beins
Environmental Working Group
Washington, DC, USA
kaley.beins@ewg.org

David Q. Andrews
Environmental Working Group
Washington, DC, USA
dandrews@ewg.org

Elizabeth Bondi-Kelly
University of Michigan
Ann Arbor, Michigan, USA
ecbk@umich.edu

Abstract

Per- and polyfluoroalkyl substances (PFAS) are persistent environmental contaminants with significant public health impacts, yet large-scale monitoring remains severely limited due to the high cost and logistical challenges of field sampling. The lack of samples leads to difficulty simulating their spread with physical models and limited scientific understanding of PFAS transport in surface waters. Yet, rich geospatial and satellite-derived data describing land cover, hydrology, and industrial activity are widely available. We introduce FOCUS, a geospatial deep learning framework for PFAS contamination mapping that integrates sparse PFAS observations with large-scale environmental context, including priors derived from hydrological connectivity, land cover, source proximity, and sampling distance. These priors are integrated into a principled, noise-aware loss, yielding a robust training objective under sparse labels. Across extensive ablations, robustness analyses, and real-world validation, FOCUS consistently outperforms baselines including sparse segmentation, Kriging, and pollutant transport simulations, while preserving spatial coherence and scalability over large regions. Our results demonstrate how AI can support environmental science by providing screening-level risk maps that prioritize follow-up sampling and help connect potential sources to surface-water contamination patterns in the absence of complete physical models.

1 Introduction

PFAS, or per- and polyfluoroalkyl substances, are persistent “forever chemicals” widely used in industrial and consumer products such as non-stick cookware, waterproof textiles, and firefighting foams [38]. Due to their extreme chemical stability, PFAS resist degradation and are now pervasive across environmental compartments, accumulating in surface and groundwater [26, 47], soils [9], and living organisms [14]. This widespread environmental presence has direct public health consequences, with 97% of Americans exhibiting detectable levels in their blood [4] and exposure linked to cancers, liver damage, and developmental disorders [33]. However, measuring PFAS concentrations remains expensive—often costing hundreds of

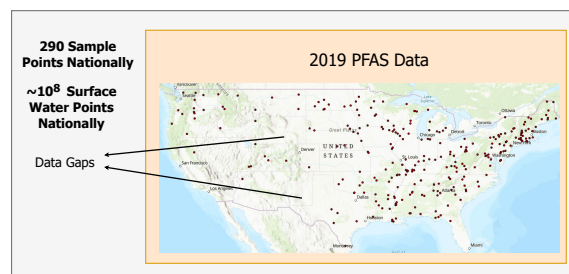


Figure 1: Illustration of limited PFAS contamination data [59]

U.S. dollars per sample—resulting in sparse and unevenly distributed ground-truth data (Fig. 1). This data scarcity leaves substantial uncertainty in identifying contamination hotspots and prioritizing targeted remediation to best protect public health.

Artificial intelligence (AI) presents a promising avenue for addressing complex health and environmental issues, including identifying PFAS hotspots. In various domains, AI has proven effective at automating labor-intensive tasks and synthesizing domain expertise, whether in land cover mapping [43], agricultural optimization [25], disease prediction [2], or environmental and Earth-system inference tasks [6, 42]. In the domain of PFAS contamination prediction, however, prior work has largely relied on tabular ML models such as random forests [3] and XGBoost [5], which aggregate environmental features around sparse sample points and discard spatial structure. For example, [10] uses a random forest model with features aggregated within a 5 km buffer around each sample (Fig. 2). Building on these efforts, we instead frame PFAS prediction as a geospatial deep learning (DL) task that operates directly on raster inputs, preserving spatial dependencies while reducing the need for manual feature engineering and aggregation.

Our contributions in this work are summarized as follows:

- We propose FOCUS, a principled noise-aware geospatial learning framework comprising a hydrology informed noise-aware objective that combines hydrological priors into a

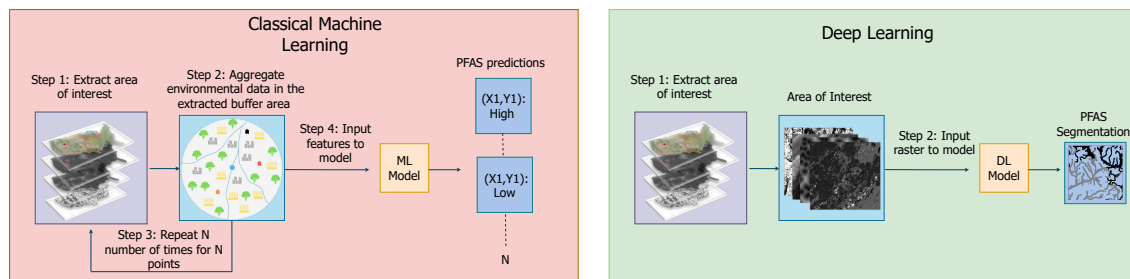


Figure 2: Left: Classical ML techniques aggregate surrounding pixel data to predict contamination at specific points (depicted as x, y coordinates); Right: DL methods process raster images directly to generate dense PFAS contamination maps in a single pass.

focal-style loss to train robust segmentation models from sparse, noisy PFAS measurements.

- We formalize PFAS surface-water mapping as learning under *structured, spatially dependent label noise* induced by expanding point measurements to pixel-level supervision.
- We derive a theoretical result showing that FOCUS optimizes a valid surrogate objective under asymmetric, pixel-wise label noise, providing a principled justification for the proposed training loss.
- We construct pixel-wise confidence weights from hydrological flow, industrial discharge proximity, land cover, and sampling distance, linking environmental processes to robust learning.
- We evaluate on real PFAS field data across the United States and benchmark against geostatistical methods, pollutant transport simulations, and tabular ML baselines, demonstrating improved predictive performance and scalability.

Domain co-design and motivation. PFAS mapping poses domain-specific challenges that limit both traditional modeling and off-the-shelf ML: sparse and biased measurements, expensive and uncertain physical simulations, and heavy reliance on manual feature engineering and spatial aggregation. We developed FOCUS in close collaboration with **environmental scientists from the Environmental Working Group, academic researchers specializing in water quality models and environmental chemistry, and an advisory group with representatives from other nonprofits and agencies such as the Huron River Watershed Council (HRWC)**, who helped shape both the model inputs (e.g., hydrology, land cover, source proximity) and the learning objective to reflect real scientific uncertainty and regulatory priorities. This co-design process informed our choice to operate directly on geospatial rasters, and to encode physically motivated correctness priors.

Reproducibility. Code, processed datasets, and scripts to reproduce the FOCUS experiments are available in the accompanying repository¹.

2 Related Work

We now summarize existing research about PFAS, spanning analytical methods from scientific domains, to emerging computational approaches, including AI techniques. We also discuss AI techniques for geospatial and sparse data.

¹Code available at https://anonymous.4open.science/r/FOCUS_KDD-D184/README.md.

Current Ways to Measure and Predict PFAS. The measurement of PFAS relies on laboratory-based analysis of water, fish tissue, and human blood samples with techniques such as liquid chromatography-tandem mass spectrometry (LC-MS) [49]. PFAS monitoring efforts have made use of such measurement techniques and beyond. For example, states such as Colorado have implemented water testing, treatment grants, and regulatory measures since 2016 [7]. In addition, there are community-based water sampling initiatives such as volunteer sampling by the Sierra Club [50] and focused efforts by organizations like the Ecology Center [12]. A recent study further underscores the importance of these efforts, revealing associations between PFAS contamination in drinking water and higher COVID-19 mortality rates in the U.S. [30]. Resources like the PFAS-Tox Database [40] also assist communities in monitoring PFAS. While highly accurate and important, laboratory-based PFAS measurements are costly, time-intensive, and difficult to scale spatially [11].

Various modeling approaches have been explored to predict contaminant distribution. Hydrological models such as SWAT [52] and MODFLOW [54] simulate pollutant transport using environmental parameters like flow rates, land use, and weather conditions. While effective, these models require extensive data and are computationally expensive at large scales [64]. Kriging, a geostatistical interpolation technique, has been widely used for mapping pollutants, including in soil [27] and groundwater [51]. Though useful in data-sparse environments, Kriging relies on simplifying assumptions such as spatial continuity and stationarity [18] that may not hold for complex contaminants like PFAS, whose transport dynamics and uncertainties are more intricate (see Section 5). Complementing these efforts, Salvatore et al. [46] proposed a “presumptive contamination” model that estimates PFAS presence based solely on proximity to known PFAS-using or -producing facilities. We aim to contribute to monitoring and modeling efforts by providing scalable, data-driven PFAS predictions.

AI Approaches for PFAS Prediction. Recent advances in AI and geospatial modeling have opened new avenues for tackling the scalability challenges of PFAS detection. For example, DeLuca et al. [10] used random forests to predict PFAS contamination in fish tissue in the Columbia River Basin, leveraging geospatial data from industrial and military facilities. On a national scale, the USGS applied XGBoost to forecast PFAS occurrence in groundwater [53] using PFAS sources, groundwater recharge, etc. Such approaches require extensive manual feature engineering, such as aggregating data spatially before prediction is possible (Fig. 2). In addition to

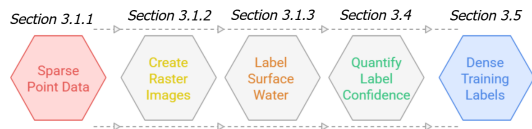


Figure 3: Overview of dataset curation pipeline

being resource-intensive (see Section 5), this preprocessing loses spatial context.

Geospatial Models. Recent advances in geospatial deep learning have introduced foundation models trained on large-scale satellite datasets for improved spatial prediction. Neural operators and physics-informed models target PDE systems [24, 29]; however, PFAS transport lacks reliable governing physics and dense simulations, motivating a noise-aware, data-driven geospatial approach. Models like Prithvi [1] and SatMAE [8] use masked autoencoders (MAE) to learn generalizable spatial representations in a semi-supervised manner, leveraging both labeled and unlabeled data. Unlike traditional ML approaches that require extensive feature engineering (e.g., Fig. 2), these models process raster (image) data directly, preserving spatial dependencies. However, many of these approaches assume that key information is directly observable in satellite imagery, which is not the case for PFAS pollution (see Section 5). We therefore adapt Prithvi to use preprocessed, proxy features, such as land cover.

Addressing Data Scarcity. In environmental data analysis, limited ground truth often necessitates pseudo- or augmented labels, which can introduce noise and lead to overfitting [45]. Various strategies have been proposed to mitigate these issues, including label smoothing and robust loss functions (e.g., Huber loss [19], Generalized Cross-Entropy [63], bootstrapping loss [41]), and focal loss [31]. Among these, focal loss is particularly effective for addressing class imbalance by down-weighting well-classified examples and focusing the model’s learning on hard, uncertain samples. Weakly supervised methods like the FESTA loss [23] further aim to capture spatial and feature relationships. FESTA is specifically designed for segmentation of remote sensing images using sparse annotations assuming spatial continuity, which may not hold for PFAS (see Section 5). Moreover, limited understanding of PFAS hydrological processes complicates the use of transfer and active learning, making it difficult to estimate uncertainty and identify reliable proxies [21, 44]. These challenges underscore the need for methods that integrate domain-specific knowledge directly into the training process.

3 Methodology

PFAS mapping presents unique challenges: labels exist only at sparse monitoring locations, yet contamination spreads via hydrological and land-use processes. To address this, we propose FOCUS as a geospatial learning framework with a noise-aware objective grounded in a latent contamination model and hydrology-informed pixel correctness priors. We perform segmentation on surface water area, classifying them as having PFAS concentrations above or below established health advisory thresholds using geospatial data.

3.1 Dataset

To contextualize our data preparation pipeline, Fig. 3 illustrates how ground truth samples are integrated with geospatial data to create the final dataset.

3.1.1 Ground Truth Samples. We use a combination of datasets and health advisories from government agencies in the United States, for both water and fish tissue samples. These are summarized in Table 1 (details in appendix).

Table 1: Datasets used for training, testing, and real-world validation.

Type	Use	Data Source	Total Size
Fish	Train/Test	EPA [58, 59]	866
Fish	Validation	MPART [35]	114
Water	Train/Test	MPART [34]	293
Water	Validation	Sampled by Authors	8

We use both fish and water samples: fish reflect longer-term accumulation relevant to exposure risk, while water samples capture localized contamination at a given time [13]. Our analysis primarily uses fish data due to the nationally representative extent.

Furthermore, PFAS concentrations are measured as continuous values in these samples, with individual measurements for different species of PFAS. We binarize PFAS concentration measurements into above (1) or below (0) health advisory thresholds, such as the EPA’s Fish and Shellfish Advisory Program health thresholds [57]. In particular, we use the cumulative metric called the Hazard Index, which assesses combined risk from individual PFAS compounds by summing their concentration-to-threshold ratios [55]. Note that for fish train/test data, this yields 775 above-threshold (89.5%) and 91 below-threshold (10.5%) samples, reflecting a critical real-world imbalance. For completeness, we also experimented with an alternative labeling scheme using three classes (see appendix).

3.1.2 Raster Image Generation. To spatially integrate the data for training and testing, multi-channel raster images were generated around each sample point (see Fig 5). Each image is a $P \times P$ pixels patch with 30-meter resolution, centered on the geographic coordinates of a sample point, where the optimal value of P is determined in Section 4.3. Once trained, the model can make predictions at any location simply by extracting and processing the corresponding raster, which is done for real-world validation.

These raster images integrate several key features. First, we incorporate readily available rasters such as the National Land Cover Database (NLCD) [61], and flow direction rasters that capture hydrological connectivity using the D8 algorithm in ArcGIS Pro [16]. In addition, we include discharger location data obtained from the U.S. EPA Enforcement and Compliance History Online (ECHO) [56] and convert them into distance rasters using a distance transform [48].

3.1.3 Ground Truth Masks. Our goal is to perform segmentation to predict PFAS contamination in surface water, but we have sparse point-level contamination measurements rather than dense labels across rasters. To generate dense training labels, every surface water pixel in a patch is labeled according to the point-level sample

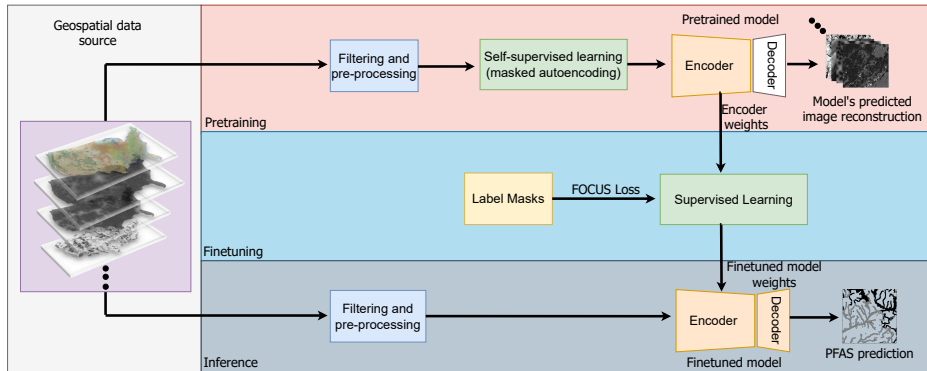


Figure 4: Model overview: high-level representation of FOCUS

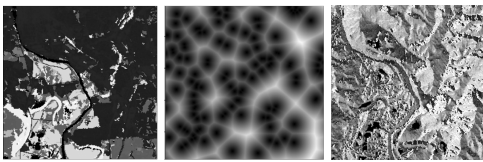


Figure 5: Example raster channels: (left) land cover, (center) distances from chemical manufacturing industries, and (right) flow direction.

measurement in that patch (i.e., if the sample point indicates PFAS above the safety thresholds, all surface water pixels are labeled 1; if below, they are labeled 0). Non-surface water pixels are assigned a value of 2. This approach extends point-level data across the patch, assuming that nearby areas may have similar contamination.

3.2 Problem Setup

Let $z_i \in \{0, 1\}$ denote the latent contamination state at pixel i , and $y_i \in \{0, 1\}$ be the observed label obtained by expanding point measurements across surface water (see Section 3.1.3). Given pixel features x_i (land cover, hydrology, distance to facilities, etc.), the goal is to learn

$$\pi_\theta(x_i) = \Pr(z_i = 1 \mid x_i) \quad (1)$$

under sparse and noisy supervision.

Two challenges arise:

- (1) **Spatially-structured label noise:** contamination spreads directionally (downstream), is source-driven (industrial discharge), and varies by land use.
- (2) **Regulatory sensitivity:** false negatives pose public health risk, requiring calibrated uncertainty and high recall on positives.

3.3 Latent Noise Model

We assume per-pixel asymmetric flip noise $\eta_i < \frac{1}{2}$, where $\eta_i = \Pr(y_i \neq z_i \mid x_i)$, motivated by laboratory detection limits and geographic label propagation. The noisy likelihood is:

$$\Pr(y_i = 1 \mid x_i) = \eta_i + (1 - 2\eta_i) \pi_\theta(x_i) \quad (2)$$

Unlike classical noisy-label models that assume global or class-conditional noise rates [20, 37], we model η_i as pixel-wise and spatially varying, reflecting physical measurement limits and label

propagation rather than annotation randomness. While instance-dependent noise has been studied (e.g., Confident Learning [39]), here η_i is driven by geophysical processes and spatial structure, not inferred solely from prediction statistics.

3.4 Physically-Informed Pixel Confidence M_i Details

We estimate a correctness score $M_i \in [0, 1]$ for each training pixel using environmental priors:

$$M_i = \alpha_1 p_{\text{discharger}} + \alpha_2 p_{\text{landcover}} + \alpha_3 p_{\text{sample}} + \alpha_4 p_{\text{downstream}} \quad (3)$$

where:

- $p_{\text{discharger}}$ decays with distance to PFAS facilities,
- $p_{\text{landcover}}$ reflects industrial vs. natural land types,
- p_{sample} decays from monitoring points,
- $p_{\text{downstream}}$ increases along hydrological flow.

These terms map environmental processes to *pixelwise label correctness priors*. Weights $(\alpha_1, \alpha_2, \alpha_3, \alpha_4)$ are selected based on domain knowledge and experimental validation.

We perform an ablation study on the 2008 PFAS dataset using a grid search over 24 noise-mask configurations derived from four inputs: dischargers, land cover, flow direction, and distance to sample points. We vary their relative weights and evaluate segmentation performance across multiple metrics. The best configuration assigns 40% to dischargers, 20% to land cover, 10% to sample distance, and 30% to flow direction. These results align with domain expert guidance that emphasizes the importance of industrial activity in driving contamination patterns. Pixels at ground truth sample points labeled 1 are assigned a probability of 1, reflecting complete confidence. However, for sample points labeled 0, we account for additional uncertainty due to certain PFAS compounds having method detection limits (MDLs) that exceed advisory thresholds². Full performance results for all configurations and additional details on the environmental priors are reported in the appendix.

²In such cases, a compound may go undetected despite being present at a high-risk level. To address this, the corresponding noise mask value is down-weighted in proportion to the ratio of the advisory threshold to the MDL

3.5 FOCUS Loss

We scale focal loss by M_i to emphasize trustworthy pixels and hard cases:

$$\mathcal{L}_{\text{FOCUS}} = \frac{1}{N} \sum_{i=1}^N M_i (1-p_i)^\gamma \left[-y_i \log p_i - (1-y_i) \log(1-p_i) \right] \quad (4)$$

where N is the total number of pixels, and p_i is the predicted probability of the positive class. Key components:

- M_i down-weights uncertain pixels (noise-robust)
- $(1-p_i)^\gamma$ up-weights hard examples (focal modulation)

Proposition 1 (Noise-Aware Surrogate Objective)

Let $z_i \in \{0, 1\}$ denote the latent contamination state and $y_i \in \{0, 1\}$ the observed expanded label under a pixel-specific asymmetric flip noise rate $\eta_i < \frac{1}{2}$, such that

$$\Pr(y_i = 1 \mid x_i) = \eta_i + (1 - 2\eta_i) \pi_\theta(x_i).$$

Then there exist coefficients a_i, b_i such that the noisy negative log-likelihood satisfies

$$\ell_{\text{noisy}}(p_i, y_i) \leq a_i \cdot \text{CE}(p_i, y_i) + b_i.$$

where CE denotes the standard cross-entropy loss. Setting $a_i = M_i$, where M_i increases as η_i decreases, yields a valid surrogate objective whose expectation upper-bounds the $\ell_{\text{noisy}}(p_i, y_i)$ and serves as a lower-bound surrogate to the clean log-likelihood.

Proof sketch. Under the asymmetric flip noise model with pixel-specific noise rate $\eta_i < \frac{1}{2}$, the noisy likelihood satisfies

$$\Pr(y_i = 1 \mid x_i) = \eta_i + (1 - 2\eta_i) p_i,$$

where $p_i = \pi_\theta(x_i)$. The corresponding negative log-likelihood is

$$\ell_{\text{noisy}}(p_i, y_i) = -\log(\eta_i + (1 - 2\eta_i) p_i).$$

Since the logarithm is concave, for any fixed anchor $p_0 \in (0, 1)$ there exist coefficients a_i, b_i such that

$$\ell_{\text{noisy}}(p_i, y_i) \leq a_i \cdot \text{CE}(p_i, y_i) + b_i,$$

We then apply the standard focal modulation $(1-p_i)^\gamma$, where $\gamma \geq 0$ controls the focus on hard examples, to the CE term.

If we set $a_i = M_i$, where M_i increases as η_i decreases (i.e., higher label trust), then $\mathcal{L}_{\text{FOCUS}}$ is a valid upper-bounding surrogate of $\mathbb{E}[\ell_{\text{noisy}}]$ (up to additive constants).

Consequently, minimizing $\mathcal{L}_{\text{FOCUS}}$ maximizes a lower bound on the (noisy) log-likelihood, and—under the alignment assumption on M_i —serves as a principled surrogate for learning from the underlying clean labels while encoding physically grounded priors rather than learned heuristics. Further details and a formal derivation are provided in the appendix.

3.6 Model

Our framework, FOCUS, is inspired by the Prithvi architecture [1] and employs a masked autoencoder (MAE) approach for pretraining (Fig. 4). Instead of relying on Prithvi’s pretrained weights, we pretrain our model on derived geospatial data products (e.g., land

cover and distance rasters), which we hypothesize offer more contextual information for capturing the environmental nuances critical to PFAS contamination prediction (see Section 5).

4 Experiments

4.1 Baselines

To contextualize our proposed framework for PFAS contamination prediction, we introduce several baseline approaches commonly employed in the field:

- **Pollutant transport simulation:** A scientific, process-based approach that models contaminant movement using hydrological principles [52]. Further details on implementation in appendix.
- **Landsat-based method:** Uses the original Prithvi weights to predict PFAS from raw satellite imagery (Landsat 7 multispectral [62]).
- **FESTA loss approach:** A state-of-the-art method for sparse segmentation from point supervision. [23].
- **Kriging:** A geostatistical interpolation method [17] that predicts contamination based on spatial relationships between points. Further details on implementation in appendix.
- **Random forest:** Closely following the methodology of [10], this model aggregates environmental features within a 5 km buffer around each sample (e.g., calculating the percentage of various land cover types) to predict contamination at individual points.
- **Rule-based approach:** Assigns contamination labels based on predefined environmental heuristics only, replicating our noise mask approach to compute a contamination probability (but without $(p_{\text{sample_dist}})$), which is then thresholded to yield binary labels.

4.2 Training Configuration

We now describe our experimental setup, with additional details in the appendix. We conduct experiments *per year* to evaluate **the model’s ability to fill spatial data gaps, an important stakeholder need**. We do not forecast across time as longitudinal ground truth is currently too sparse and inconsistent for reliable temporal supervision. For each year, we split the data into 80% training and 20% testing, with geographically disjoint regions to avoid spatial leakage and ensure diversity.

We use a batch size of 4 to preserve the stability of the pretrained backbone and optimize with AdamW [32] ($\beta_1 = 0.9$ and $\beta_2 = 0.999$). A custom learning-rate schedule with warmup followed by polynomial decay stabilizes convergence and enables gradual adaptation to limited data. Hyperparameters were selected based on consistent convergence.

4.3 Ablation Study

We conduct ablation studies across the following dimensions:

- **Noise Weights:** We evaluate the impact of incorporating noise masks into the FOCUS loss function. With noise masks, pixel-wise confidence scores scale focal loss to emphasize high-confidence pixels; without them, the loss reduces to standard focal loss [31].

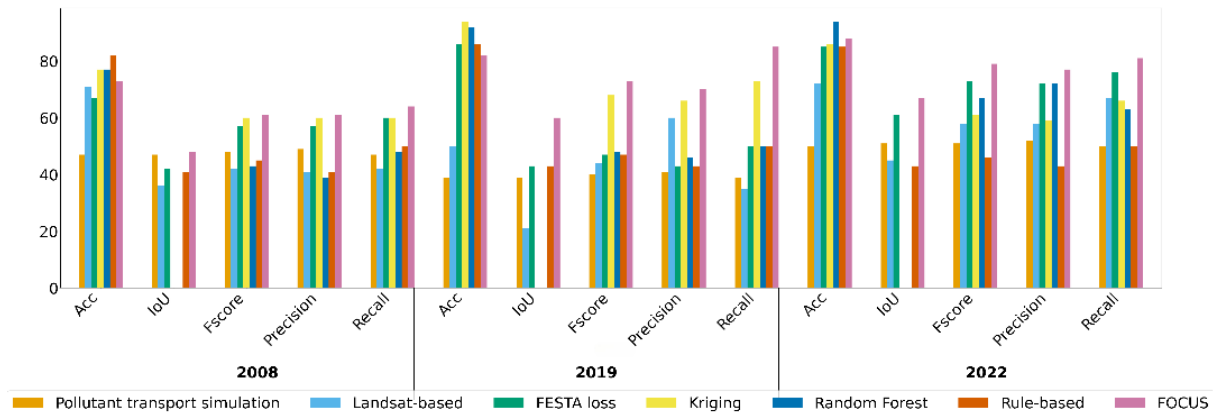


Figure 6: Comparison of performance across different methods and years. Results are averaged over 3 random seeds for FOCUS and applicable baselines (Landsat-based, FESTA loss, rule-based). IoU is not applicable to methods that do not produce dense pixel-level segmentations (e.g., Kriging and Random Forest), and is therefore omitted for those approaches.

- Raster Size:** To understand the influence of spatial context, we compare raster patches of 512×512 and 256×256 pixels. Larger patches capture broader context, potentially including contamination sources farther from the sample point, while smaller patches reduce label noise and focus on localized features.

While the primary focus of this work is on PFAS contamination, we also explored the generalizability of our framework to land cover classification, and robustness through a consistency analysis detailed in the appendix.

4.4 Metrics

The reported metrics include accuracy, Intersection over Union (IoU), F-score, precision, and recall. Performance metrics in this study are reported exclusively from evaluations **using only ground truth samples**. In addition, we assess timing efficiency (in seconds) as a metric to evaluate the model’s computational scalability.

For threshold-dependent metrics, we select the decision threshold using out-of-fold predictions on the training data. Specifically, we perform K -fold cross-validation on the training set, sweep thresholds to maximize F-score on the resulting out-of-fold predictions, and apply the selected threshold to the held-out test set. We use $K = 5$ folds and sweep 200 evenly spaced thresholds in $[0, 1]$. Thresholds are selected independently for each method.

5 Results

5.1 FOCUS Outperforms Existing Baselines

5.1.1 Main Results. We first compared FOCUS against six alternative approaches for PFAS contamination prediction, as shown in Fig. 6. **Overall, FOCUS provides the most consistent performance across years and metrics.** While several baselines achieve competitive accuracy, **according to domain experts, accuracy alone is insufficient in this highly imbalanced setting, making precision–recall trade-offs more informative.** In particular, Kriging and the FESTA loss achieve comparable accuracy in some years and show reasonable performance across metrics, highlighting the strength of spatial interpolation and structure-aware learning in

this setting. The Landsat-based model yields moderate results, suggesting that satellite features alone are insufficient without explicit geospatial context. The random forest approach, despite achieving acceptable accuracy, suffered from lower F-score, precision, and recall, likely due to the limited spatial context from per-point feature aggregation. Pollutant transport simulation and the rule-based approach provide useful physics- and heuristic-driven references (the latter also serving as a component in our noise modeling), but they lag behind data-driven methods in overall predictive balance. Taken together, these results indicate that FOCUS consistently achieves a favorable trade-off between precision and recall across years, which is critical for robust large-scale environmental screening.

5.1.2 Time Efficiency. We compare FOCUS against a random forest baseline (following DeLuca et al. [10]) using similar environmental features and datasets. Table 2 reports feature extraction and inference times over a 1 km^2 area and all of Northern Michigan (NM, $\sim 44,000 \text{ km}^2$). The ML baseline requires aggregating features within a spatial buffer per point, resulting in significantly higher extraction costs at scale. In contrast, FOCUS processes full raster patches efficiently, reducing feature extraction time from days to hours over NM, while inference times remain comparable between methods. Feature extraction was performed on an Intel Xeon Gold 6154 CPU (3.0 GHz), and inference used an AMD Ryzen Threadripper PRO 7985WX with an NVIDIA RTX 6000 Ada GPU.

Table 2: Comparison of performance for feature extraction and inference using random forest and FOCUS over 1 km^2 area and Northern Michigan (NM). Results averaged over 10 runs.

	Feature extraction		Inference	
	ML	DL	ML	DL
For 1 km^2 area	1.2 ± 0.2 mins	4.7 ± 0.5 sec	0.0003 ± 0.0002 sec	0.0005 ± 0.0001 sec
For NM	2 days	$3.2 \text{ hrs} \pm 0.4 \text{ hrs}$	7.5 ± 1 sec	13 ± 2 sec

5.2 FOCUS Applies in the Real World

We next conducted two complementary validation efforts of predicted contamination maps of **new regions** – beyond regions surrounding ground truth sample points in the train and test sets – using field-collected data (see Table 1). First, our research team collected surface water samples from multiple local sites in Ann Arbor, Michigan, in mid-2025. These sites represent previously unsampled regions and provide an independent assessment of model generalization beyond our test set under sparse and biased sampling, as testing is typically limited due to cost and feasibility constraints. Notably, as shown in Fig. 7, the model, trained on 2024 surface water data from MPART, correctly identified the 8 collected points as highly contaminated, demonstrating FOCUS’s ability to generalize under severe label scarcity. We are actively pursuing larger-scale validation with stakeholders and regulators. Technical details on sample analysis are provided in the appendix. Second, we evaluated our 2019

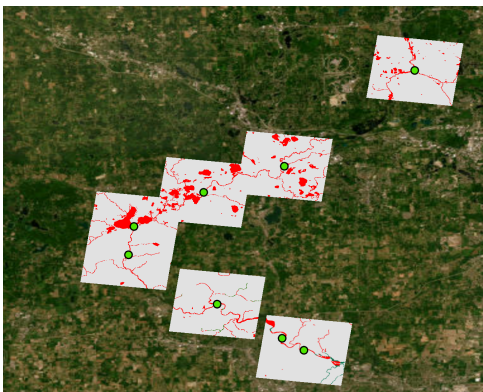


Figure 7: Real-world validation using surface water samples collected by our team. Newly sampled locations (green) are overlaid on model predictions, with red indicating areas of high predicted contamination, and dark green indicating areas of lower predicted contamination.

fish tissue model in Table 3 on the publicly available MPART fish dataset from 2019 [35], which includes PFAS measurements in fish tissue from across Michigan, collected independently from our fish train and test sets. Results are comparable to Fig. 6.

Qualitatively, Fig. 8 shows grayscale probability maps with red overlays indicating confident positive predictions in low-trust regions; the focal baseline produces many such responses, whereas FOCUS largely suppresses them, yielding more conservative behavior under unreliable supervision.

Table 3: FOCUS performance on fish tissue samples collected independently of training data. Results averaged over 3 random seeds.

Metric	Accuracy	IoU	F1	Precision	Recall
MPART Fish Samples	85 ± 2 %	60 ± 1 %	72 ± 1 %	75 ± 1 %	70 ± 2 %

5.3 FOCUS Noise Masks Improve Performance

Table 4 evaluates the effect of incorporating noise masks in FOCUS, compared to focal loss alone (i.e., removing M_i from Eq. 4). Adding noise masks consistently improves performance by emphasizing

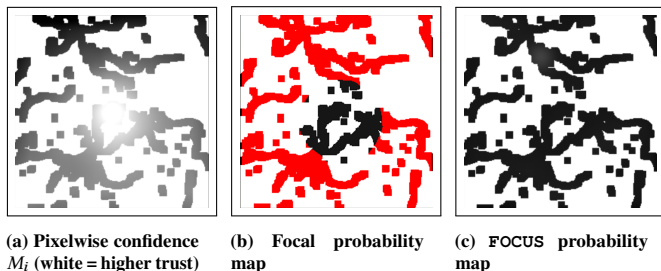


Figure 8: Grayscale PFAS probabilities (white = higher). Red overlays indicate overconfident positives in low-trust regions ($p_i \geq 0.50$, $M_i \leq 0.30$). FOCUS suppresses such responses, while the focal baseline produces many.

Table 4: Ablation showing impact of noise-aware loss (FOCUS) vs. standard focal loss. Results averaged over 3 random seeds. Bold values denote the best result per year.

Metric	2008 (%)		2019 (%)		2022 (%)	
	Focal only	FOCUS	Focal only	FOCUS	Focal only	FOCUS
Accuracy	37 ± 2	73 ± 1	62 ± 1	82 ± 1	55 ± 3	88 ± 2
IoU	22 ± 3	48 ± 2	41 ± 2	60 ± 2	36 ± 3	67 ± 2
F-score	36 ± 3	61 ± 2	57 ± 1	73 ± 2	53 ± 3	79 ± 2
Precision	54 ± 2	61 ± 2	63 ± 2	70 ± 2	63 ± 3	77 ± 2
Recall	55 ± 2	64 ± 2	78 ± 1	85 ± 1	74 ± 1	81 ± 2

high-confidence pixels and down-weighting uncertain ones during training. This ablation uses a 256×256 resolution, selected based on the patch-size study in the appendix, where it outperformed 512×512 , likely due to reduced label-noise propagation over large contexts. We did not evaluate smaller patches, as overly small contexts can degrade accuracy and increase variability [28].

5.4 FOCUS has Robust Results

To evaluate generalization to unseen regions, we perform spatial cross-validation by holding out sets of U.S. states (Table 5). Specifically, three disjoint groups of five states each are used as test sets, with the remaining states used for training, ensuring no spatial overlap and mimicking deployment in unsampled areas. FOCUS consistently outperforms focal loss across all years, demonstrating stronger spatial generalization and robustness under distribution shifts.

We also assess spatial robustness via a **consistency analysis** across all 49 continental U.S. states by comparing predictions on overlapping patches at two overlap scales (56×56 and 156×156 pixels). We observe high agreement (above 93% on average), indicating locally consistent predictions; full details are provided in the appendix. Results on model calibration (i.e., Expected Calibration Error (ECE) [22]) are also provided in the appendix, showing low ECE values (≤ 0.1) and indicating that predicted probabilities are well-aligned with observed outcomes.

6 Scientific Impact and Interdisciplinary Considerations

This work advances PFAS science by linking large-scale environmental context to surface-water contamination risk and its

Table 5: Cross-state generalization results (mean \pm std, over the disjoint state splits). Bold values denote the best result per year.

Metric	2008 (%)		2019 (%)		2022 (%)	
	Focal Only	FOCUS	Focal Only	FOCUS	Focal Only	FOCUS
Accuracy	58 \pm 2	70 \pm 1	76 \pm 1	89 \pm 1	78 \pm 2	92 \pm 1
IoU	34 \pm 2	48 \pm 1	40 \pm 2	55 \pm 1	56 \pm 2	75 \pm 1
F-score	47 \pm 1	63 \pm 1	46 \pm 2	61 \pm 1	68 \pm 1	85 \pm 1
Precision	49 \pm 2	62 \pm 1	49 \pm 3	59 \pm 2	69 \pm 2	82 \pm 1
Recall	49 \pm 2	72 \pm 1	50 \pm 1	71 \pm 2	85 \pm 1	91 \pm 1

implications for bioaccumulation. By integrating industrial dischargers, land cover, and hydrological transport with sparse measurements, our framework produces spatially consistent risk maps that help identify regions likely to be under-sampled, supporting targeted follow-up testing and more systematic risk assessment. At a broader scale, such modeling enables more consistent, nationwide perspectives on contamination risk, complementing existing, state-level fish advisory programs.

Beyond static risk mapping, our interface supports scientific exploration and hypothesis generation. From a scientific perspective, while FOCUS does not yet perform source attribution, the interface enables exploratory analysis by overlaying predicted risk with known discharger locations and hydrological context. Regions exhibiting high predicted risk despite few nearby known sources, such as the highlighted example in Fig 9, have also been noted by domain experts as areas of unexplained contamination, suggesting potential unknown, legacy, or poorly characterized sources and motivating targeted follow-up investigation.

The need for AI/ML in this domain is driven by severe data sparsity and fragmentation. PFAS comprise thousands of compounds with diverse sources and uses, yet environmental measurements—especially in surface waters and fish—remain extremely limited in space and time. Traditional monitoring and mechanistic modeling alone cannot provide comprehensive coverage, motivating learning-based approaches that integrate heterogeneous geospatial data and extrapolate risk patterns under uncertainty.

Applying AI in this setting also raises scientific and societal challenges, including interpretability, uncertainty communication, and regulatory alignment. Our approach addresses these concerns by explicitly modeling spatially structured label noise and incorporating physically informed priors, providing more calibrated and transparent predictions than standard black-box models.

7 FOCUS Web Map Interface

To support real-world use and stakeholder engagement, we have developed a web-based, interactive PFAS risk mapping interface with policymakers and domain stakeholders that visualizes model predictions at national scale (Fig. 9). The interface displays predicted PFAS contamination risk across surface waters and fish tissue using discrete risk categories (e.g., low, medium, high), enabling intuitive exploration by non-technical users.

The map integrates FOCUS predictions with contextual geospatial layers, including surface water extents, land cover, hydrological features, and known discharge locations. Users can toggle layers, zoom to regions of interest, and inspect spatial patterns across years

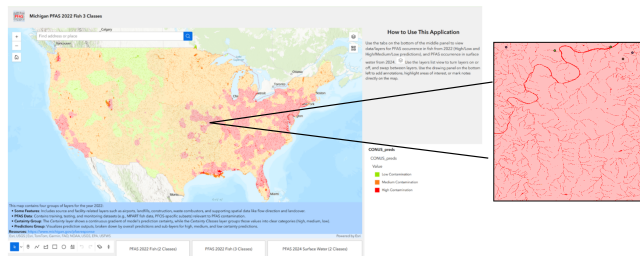


Figure 9: Web interface for exploring FOCUS predictions. The zoomed region shows high predicted risk despite few nearby known dischargers (shown as point overlays).

and data modalities. The interface was developed in collaboration with policymakers and domain stakeholders to ensure interpretability, transparency, and responsible communication of model outputs.

This deployment illustrates how noise-aware geospatial predictions can be translated into actionable decision-support tools, while acknowledging uncertainty and the limitations of sparse environmental sampling.

8 Conclusion and Future Work

We introduced FOCUS, a geospatial deep learning framework that integrates multi-channel raster inputs with a **principled noise-aware learning objective** designed for spatially structured label noise arising from point-to-pixel supervision. By combining hydrology-informed correctness priors with a noise-robust loss, FOCUS improves predictive performance while preserving spatial coherence, enabling large-scale PFAS contamination screening.

Future work will explore predictive uncertainty quantification to guide targeted sampling and enhance prediction robustness. We also aim to incorporate temporal modeling using multi-year data to track and forecast evolving PFAS patterns, as longitudinal measurements become denser and domain understanding enables more physics-informed supervision and priors. Finally, we plan to build on public contamination maps (e.g., EWG [15], [60]) by deploying our framework responsibly.

9 Limitations and Ethical Considerations

As with any large-scale environmental modeling effort, FOCUS performance is ultimately bounded by the availability and quality of underlying data. Additionally, we consider a static, one-shot prediction setting; coupling FOCUS with active or adaptive sampling is left to future work. Furthermore, the current model does not yet attribute predicted risk to specific PFAS compounds and sources, though we are actively developing extensions in this direction. Accordingly, predictions should be interpreted as screening-level risk signals to prioritize follow-up sampling rather than definitive contamination assessments.

Given the ethical implications of releasing public-facing PFAS risk maps—including impacts on public health, environmental justice, and property values—we engage an advisory group with representatives from nonprofits and agencies (e.g., HRWC). This collaboration helps tailor outputs to community needs, communicate uncertainty, and support responsible use in remediation and policy decisions.

References

- [1] Josh Blumenfeld. 2023. NASA and IBM Openly Release Geospatial AI Foundation Model for NASA Earth Observation Data | Earthdata. <https://www.earthdata.nasa.gov/news/impact-ibm-hls-foundation-model>
- [2] Elizabeth Bondi-Kelly, Haipeng Chen, Christopher D. Golden, Nikhil Behari, and Milind Tambe. 2023. Predicting micronutrient deficiency with publicly available satellite data. *AI Magazine* 44, 1 (2023), 30–40. doi:10.1002/aaai.12080
- [3] Leo Breiman. 2001. Random Forests. *Machine Learning* 45, 1 (Oct. 2001), 5–32. doi:10.1023/A:1010933404324
- [4] CDC. 2024. Centers for Disease Control and Prevention. <https://www.cdc.gov/index.html>
- [5] Tianqi Chen and Carlos Guestrin. 2016. XGBoost: A Scalable Tree Boosting System. In *Proceedings of the 22nd ACM SIGKDD International Conference on Knowledge Discovery and Data Mining*, 785–794. doi:10.1145/2939672.2939785 arXiv:1603.02754 [cs].
- [6] Sylvain Christin, Éric Hervet, and Nicolas Lecomte. 2019. Applications for deep learning in ecology. *Methods in Ecology and Evolution* 10, 10 (2019), 1632–1644. doi:10.1111/2041-210X.13256
- [7] Colorado Department of Public Health and Environment. n.d.. PFAS Action Plan. <https://cdphe.colorado.gov/chemicals-from-toxic-firefighting-foam-pfas/pfas-action-plan>
- [8] Yezhen Cong, Samar Khanna, Chenlin Meng, Patrick Liu, Erik Rozi, Yutong He, Marshall Burke, David B. Lobell, and Stefano Ermon. 2023. SatMAE: Pre-training Transformers for Temporal and Multi-Spectral Satellite Imagery. arXiv:2207.08051 (Jan. 2023). doi:10.48550/arXiv.2207.08051 arXiv:2207.08051 [cs].
- [9] Brian C. Crone, Thomas F. Speth, David G. Wahman, Samantha J. Smith, Gulizhaer Abulikemu, Eric J. Kleiner, and Jonathan G. Pressman. 2019. Occurrence of Per- and Polyfluoroalkyl Substances (PFAS) in Source Water and Their Treatment in Drinking Water. *Critical reviews in environmental science and technology* 49, 24 (June 2019), 2359–2396. doi:10.1080/10643389.2019.1614848
- [10] Nicole M. DeLuca, Ashley Mullikin, Peter Brumm, Ana G. Rappold, and Elaine Cohen Hubal. 2023. Using Geospatial Data and Random Forest To Predict PFAS Contamination in Fish Tissue in the Columbia River Basin, United States. *Environmental Science & Technology* 57, 37 (sep 2023), 14024–14035. doi:10.1021/acs.est.3c03670
- [11] Kyle Doudrick. 2024. Removing PFAS from public water will cost billions and take time • Virginia Mercury. <https://viriniamercury.com/2024/04/18/removing-pfas-from-public-water-will-cost-billions-and-take-time/>
- [12] EcoCenter. n.d.. Protecting Communities from PFAS Pollution. <https://www.ecocenter.org/our-work/protecting-communities-pfas-pollution> PFAS contamination is one of the most pressing environmental health issues we face. These chemicals impact the lives and health of millions of Americans. Per- and polyfluoroalkyl substances (PFAS) are a class of more than 12,000 different chemicals with established links to adverse health impacts. There are more than 285 sites in Michigan that have been identified as PFAS contaminated, and in the United States that number is over 6,000..
- [13] Environmental Working Group. 2023. EWG Study: Eating One Freshwater Fish Equals a Month of Drinking Water Laced with PFOS. <https://www.ewg.org/news-insights/news-release/2023/01/ewg-study-eating-one-freshwater-fish-equals-month-drinking> A new study by Environmental Working Group scientists finds that consumption of just a single serving of freshwater fish per year could be equal to a month of drinking water laced with the “forever chemical” PFOS at high levels that may be harmful..
- [14] Environmental Working Group. 2023. Forever Chemicals in Freshwater Fish: Mapping a Growing Environmental Justice Crisis. <https://www.ewg.org/news-insights/news/2023/01/forever-chemicals-freshwater-fish-mapping-growing-environmental-justice> Accessed: 2025-07-27.
- [15] Environmental Working Group. 2024. Interactive Map: PFAS Contamination Crisis: New Data Show 8,865 Sites in 50 States. <http://www.ewg.org/interactive-maps/pfas-contamination/map/>
- [16] Esri. 2024. Flow Direction (Spatial Analyst) — ArcGIS Pro Documentation. <https://pro.arcgis.com/en/pro-app/latest/tool-reference/spatial-analyst/flow-direction.htm>. Accessed: 2025-07-17.
- [17] Esri. n.d.. How Kriging Works — ArcGIS Pro Documentation. <https://pro.arcgis.com/en/pro-app/latest/tool-reference/3d-analyst/how-kriging-works.htm> Accessed: 2025-07-27.
- [18] GISGeography. 2017. Kriging Interpolation - The Prediction Is Strong in this One. <https://gisgeography.com/kriging-interpolation-prediction/>
- [19] Kaan Gokcesu and Hakan Gokcesu. 2021. Generalized Huber Loss for Robust Learning and its Efficient Minimization for a Robust Statistics. arXiv:2108.12627 (Aug. 2021). doi:10.48550/arXiv.2108.12627 arXiv:2108.12627 [stat].
- [20] Jacob Goldberger and Ehud Ben-Reuven. 2017. Training deep neural-networks using a noise adaptation layer. <https://openreview.net/forum?id=H12GRgxcg>
- [21] Jennifer L. Guelfo, Stephen Korzeniowski, Marc A. Mills, Janet Anderson, Richard H. Anderson, Jennifer A. Arblaster, Jason M. Conder, Ian T. Cousins, Kavitha Dasu, Barbara J. Henry, Linda S. Lee, Jinxia Liu, Erica R. McKenzie, and Janice Willey. 2021. Environmental Sources, Chemistry, Fate, and Transport of Per- and Polyfluoroalkyl Substances: State of the Science, Key Knowledge Gaps, and Recommendations Presented at the August 2019 SETAC Focus Topic Meeting. *Environmental Toxicology and Chemistry* 40, 12 (Dec. 2021), 3234–3260. doi:10.1002/etc.5182
- [22] Chuan Guo, Geoff Pleiss, Yu Sun, and Kilian Q. Weinberger. 2017. On Calibration of Modern Neural Networks. arXiv:1706.04599 (Aug. 2017). doi:10.48550/arXiv.1706.04599 arXiv:1706.04599 [cs].
- [23] Yuansheng Hua, Diego Marcos, Lichao Mou, Xiao Xiang Zhu, and Devis Tuia. 2022. Semantic Segmentation of Remote Sensing Images with Sparse Annotations. *IEEE Geoscience and Remote Sensing Letters* 19 (2022), 1–5. doi:10.1109/LGRS.2021.3051053 arXiv:2101.03492 [cs].
- [24] George Em Karniadakis, Ioannis G. Kevrekidis, Lu Lu, Paris Perdikaris, Sifan Wang, and Liu Yang. 2021. Physics-informed machine learning. *Nature Reviews Physics* 3, 6 (June 2021), 422–440. doi:10.1038/s42254-021-00314-5
- [25] Hannah Kerner, Catherine Nakalembe, Adam Yang, Ivan Zvonkov, Ryan McWeeny, Gabriel Tseng, and Inbal Becker-Reshef. 2024. How accurate are existing land cover maps for agriculture in Sub-Saharan Africa? *Scientific Data* 11, 1 (May 2024), 486. doi:10.1038/s41597-024-03306-z
- [26] Blake Langenbach and Mark Wilson. 2021. Per- and Polyfluoroalkyl Substances (PFAS): Significance and Considerations within the Regulatory Framework of the USA. *International Journal of Environmental Research and Public Health* 18, 21 (Oct. 2021), 11142. doi:10.3390/ijerph182111142
- [27] Fatima-Zohra Benmost Largueche. 2006. Estimating Soil Contamination with Kriging Interpolation Method. *American Journal of Applied Sciences* 3, 6 (June 2006), 1894–1898. doi:10.3844/ajassp.2006.1894.1898
- [28] Alex Mark Lechner, Alfred Stein, Simon D. Jones, and Jelle Garke Ferwerda. 2009. Remote sensing of small and linear features: quantifying the effects of patch size and length, grid position and detectability on land cover mapping. *Remote Sensing of Environment* 113, 10 (Oct. 2009), 2194–2204. doi:10.1016/j.rse.2009.06.002
- [29] Zongyi Li, Nikola Kovachki, Kamyar Aizzadenesheli, Burigede Liu, Kaushik Bhattacharya, Andrew Stuart, and Anima Anandkumar. 2020. Fourier Neural Operator for Parametric Partial Differential Equations. <https://arxiv.org/abs/2010.08895v3>
- [30] Jahred M. Liddie, Marie-Abèle Bind, Mahesh Karra, and Elsie M. Sunderland. 2024. County-level associations between drinking water PFAS contamination and COVID-19 mortality in the United States. *Journal of Exposure Science & Environmental Epidemiology* (Oct. 2024), 1–8. doi:10.1038/s41370-024-00723-5
- [31] Tsung-Yi Lin, Priya Goyal, Ross Girshick, Kaiming He, and Piotr Dollár. 2018. Focal Loss for Dense Object Detection. arXiv:1708.02002 (Feb. 2018). doi:10.48550/arXiv.1708.02002 arXiv:1708.02002 [cs].
- [32] Ilya Loshchilov and Frank Hutter. 2019. Decoupled Weight Decay Regularization. arXiv:1711.05101 (Jan. 2019). doi:10.48550/arXiv.1711.05101 arXiv:1711.05101 [cs].
- [33] Katherine E. Manz. 2024. Considerations for Measurements of Aggregate PFAS Exposure in Precision Environmental Health. *ACS Measurement Science Au* 4, 6 (Dec. 2024), 620–628. doi:10.1021/acsmeasuresciau.4c00052
- [34] Michigan Department of Environment, Great Lakes, and Energy. 2023. PFAS Surface Water Sampling. https://gis-egle.hub.arcgis.com/datasets/391cca4f364845829abcd5a92093c631_1/about Accessed: 2025-07-27.
- [35] Michigan Department of Environment, Great Lakes, and Energy. 2025. Michigan Fish Contaminant Monitoring Sampling Sites and Select Results (Consolidated). <https://gis-egle.hub.arcgis.com/maps/d4bbb519842c44638eeb9a15461c441f/about> Accessed: 2025-07-27.
- [36] Michigan Department of Health and Human Services. n.d.. Find Your Area – Eat Safe Fish Guidelines. <https://www.michigan.gov/mdhhs/safety-injury-prevention/environmental-health/topics/eatsafefish/find-your-area>. Accessed: 2026-02-05.
- [37] Nagarajan Natarajan, Inderjit S Dhillon, Pradeep K Ravikumar, and Ambuj Tewari. 2013. Learning with Noisy Labels. In *Advances in Neural Information Processing Systems*, Vol. 26. Curran Associates, Inc. https://papers.nips.cc/paper_files/paper/2013/hash/3871bd64012152bfb53fd04b401193f-Abstract.html
- [38] National Institute of Environmental Health Sciences. n.d.. Perfluoroalkyl and Polyfluoroalkyl Substances (PFAS). <https://www.niehs.nih.gov/health/topics/agents/pfc>. Accessed: 2025-07-27.
- [39] Curtis Northcutt, Lu Jiang, and Isaac Chuang. 2021. Confident Learning: Estimating Uncertainty in Dataset Labels. *J. Artif. Int. Res.* 70 (May 2021), 1373–1411. doi:10.1613/jair.1.12125
- [40] Katherine E. Pelch, Anna Reade, Carol F. Kwiatkowski, Francheska M. Merced-Nieves, Haleigh Cavalier, Kim Schultz, Taylor Wolffe, and Julia Varshavsky. 2022. The PFAS-Tox Database: A systematic evidence map of health studies on 29 per- and polyfluoroalkyl substances. *Environment International* 167 (Sept. 2022), 107408. doi:10.1016/j.envint.2022.107408
- [41] Scott Reed, Honglak Lee, Dragomir Angelov, Christian Szegedy, Dumitru Erhan, and Andrew Rabinovich. 2015. Training Deep Neural Networks on Noisy Labels with Bootstrapping. arXiv:1412.6596 (April 2015). doi:10.48550/arXiv.1412.6596 arXiv:1412.6596 [cs].

- [42] Markus Reichstein, Gustau Camps-Valls, Bjorn Stevens, Martin Jung, Joachim Denzler, Nuno Carvalhais, and Prabhath. 2019. Deep learning and process understanding for data-driven Earth system science. *Nature* 566, 7743 (Feb. 2019), 195–204. doi:10.1038/s41586-019-0912-1
- [43] Caleb Robinson, Anthony Ortiz, Kolya Malkin, Blake Elias, Andi Peng, Dan Morris, Bistra Dilkina, and Nebojsa Jojic. 2020. Human-Machine Collaboration for Fast Land Cover Mapping. *Proceedings of the AAAI Conference on Artificial Intelligence* 34, 0303 (April 2020), 2509–2517. doi:10.1609/aaai.v34i03.5633
- [44] Stefania Russo, Moritz Lüurig, Wenjin Hao, Blake Matthews, and Kris Villez. 2020. Active Learning for Anomaly Detection in Environmental Data. *Environmental Modelling & Software* 134 (Dec. 2020), 104869. doi:10.1016/j.envsoft.2020.104869
- [45] Anastasiia Safonova, Gohar Ghazaryan, Stefan Stiller, Magdalena Main-Knorn, Claas Nendel, and Masahiro Ryo. 2023. Ten Deep Learning Techniques to Address Small Data Problems with Remote Sensing. *International Journal of Applied Earth Observation and Geoinformation* 125 (Dec. 2023), 103569. doi:10.1016/j.jag.2023.103569
- [46] Derrick Salvatore, Kira Mok, Kimberly K. Garrett, Grace Poudrier, Phil Brown, Linda S. Birnbaum, Gretta Goldenman, Mark F. Miller, Sharyle Patton, Maddy Poehlein, Julia Varshavsky, and Alissa Corder. 2022. Presumptive Contamination: A New Approach to PFAS Contamination Based on Likely Sources. *Environmental Science & Technology Letters* 9, 11 (nov 2022), 983–990. doi:10.1021/acs.estlett.2c00502
- [47] Tim Schroeder, David Bond, and Janet Foley. 2021. PFAS soil and groundwater contamination via industrial airborne emission and land deposition in SW Vermont and Eastern New York State, USA. *Environmental Science. Processes & Impacts* 23, 2 (March 2021), 291–301. doi:10.1039/d0em00427h
- [48] SciPy Developers. 2019. distance_transform_edt — SciPy v1.16.0 Manual. https://docs.scipy.org/doc/scipy-1.16.0/reference/generated/scipy.ndimage.distance_transform_edt.html. https://docs.scipy.org/doc/scipy-1.16.0/reference/generated/scipy.ndimage.distance_transform_edt.html Accessed: 2025-07-27.
- [49] J. Shoemaker and D. Tettenhorst. 2020. Method 537.1 Determination of Selected Per- and Polyfluorinated Alkyl Substances in Drinking Water by Solid Phase Extraction and Liquid Chromatography/Tandem Mass Spectrometry (LC/MS/MS). https://cfpub.epa.gov/si/si_public_record_report.cfm?dirEntryId=348508&Lab=CESER&simpleSearch=0&showCriteria=2&searchAll=537.1&TIMSType=&dateBeginPublishedPresented=03%2F24%2F2018
- [50] Sierra Club. n.d.. Community Science Testing for PFAS in Water or Biosolids. <https://www.sierraclub.org/grassroots-network/pfas/community-science-testing-pfas-water-or-biosolids> Community science to test for PFAS in rivers and lakes and in sludge/biosolids.
- [51] Prafull Singh and Pradiptika Verma. 2019. *A Comparative Study of Spatial Interpolation Technique (IDW and Kriging) for Determining Groundwater Quality*. Elsevier, 43–56. doi:10.1016/B978-0-12-815413-7.00005-5
- [52] SWAT. n.d.. Soil & Water Assessment Tool. <https://swat.tamu.edu/>
- [53] Andrea K. Tokranov, Laura M. Bexfield, Katherine M. Ransom, James A. Kingsbury, Miranda S. Fram, Elise Watson, Danielle I. Dupuy, Stefan Voss, Bryant C. Jurgens, Paul E. Stackelberg, Delicia Beaty, and Kelly Smalling. 2023. Predictions of PFAS in groundwater used as a source of drinking water and related data in the conterminous United States. doi:10.5066/P93RXTKJ Creative Commons Zero v1.0 Universal.
- [54] K. Torcoletti. 2012. What is MODFLOW? <https://www.waterloohydrogeologic.com/2012/06/22/what-is-modflow/> Published by Waterloo Hydrogeologic. Accessed: 2025-07-27.
- [55] U.S. Environmental Protection Agency. 2023. How Do I Calculate the Hazard Index? https://www.epa.gov/system/files/documents/2023-03/How%20do%20I%20calculate%20the%20Hazard%20Index._3.14.23.pdf EPA Fact Sheet, March 14.
- [56] U.S. Environmental Protection Agency. n.d.. Water Pollution Search | ECHO | US EPA. <https://echo.epa.gov/trends/loading-tool/water-pollution-search>
- [57] U.S. EPA. 2024. Contaminants to Monitor in Fish and Shellfish Advisory Programs: Compilation of Peer Review-Related Information. (2024).
- [58] OW US EPA. 2024. 2022 National Lakes Assessment - Fish Tissue Study. <https://www.epa.gov/choose-fish-and-shellfish-wisely/2022-national-lakes-assessment-fish-tissue-study>
- [59] U.S. EPA, OW. 2015. National Rivers and Streams Assessment. <https://www.epa.gov/national-aquatic-resource-surveys/nrsa>
- [60] U.S. Geological Survey. 2023. <https://www.usgs.gov/tools/pfas-us-tapwater-interactive-dashboard>
- [61] U.S. Geological Survey. 2024. National Land Cover Database | U.S. Geological Survey. <https://www.usgs.gov/centers/eros/science/annual-national-land-cover-database>
- [62] U.S. Geological Survey. n.d.. Landsat 7 Level 2, Collection 2, Tier 1 | Earth Engine Data Catalog. https://developers.google.com/earth-engine/datasets/catalog/LANDSAT_LE07_C02_T1_L2
- [63] Zhilu Zhang and Mert R. Sabuncu. 2018. Generalized Cross Entropy Loss for Training Deep Neural Networks with Noisy Labels. arXiv:1805.07836 (Nov. 2018). doi:10.48550/arXiv.1805.07836 arXiv:1805.07836 [cs].
- [64] Wei Zhi, Alison P Appling, Heather E Golden, Joel Podgorski, and Li Li. 2024. Deep learning for water quality. *Nature Water* 2, 3 (2024), 228–241.

10 Appendix

To help navigate the appendix, Table 6 provides an overview linking each appendix subsection to the corresponding sections in the main paper where they are mentioned or expanded upon.

Table 6: Mapping between appendix sections and corresponding references in the main paper.

appendix Subsection	Referenced in Main Paper Section(s)
A. Model Calibration	Section 5.4
B. Physically-Informed Pixel Confidence M_i Details	Section 3.4
C. Kriging	Section 4.1
D. Pollutant Transport Simulation	Section 4.1
E. Consistency Analysis	Section 5.4
F. Evaluating the Impact of Noise Masks on Segmentation of Land Cover Types	Section 4.3
G. Dataset	Section 3.1
H. FOCUS Per-Class Results	-
I. Ternary Classification of Hazard Levels	Section 3.1.1
J. Statistical Significance of Performance Gains	-
K. Distance-to-Industry Rasters.	Section 3.1.2
L. Ablation Results for Image Resolution	Section 4.3
M. Hyperparameter Tuning and Selection	Section 4.2
N. Technical Details on Sample Analysis and Training Data for Real-World Predictions	Section 5.2
O. FOCUS Loss Derivation and Assumptions	Section 3.5
P. Region-Level Risk Signals and Bioaccumulation Evidence	-

A Model Calibration

We evaluated model calibration using ECE, which quantifies the discrepancy between predicted probabilities and observed outcomes where lower scores indicate better calibration. Table 7 shows the ECE scores for our model trained with FOCUS loss for the years 2008, 2019, and 2022.

The very low ECE values, that is, 0.1 for 2008 and 2019, and 0.07 for 2022, demonstrate that our model’s predicted probabilities

Table 7: ECE Scores for Models Trained with FOCUS Loss Across Different Years.

Metric	2008	2019	2022
ECE Score	0.1	0.1	0.07

are closely aligned with the observed outcomes, indicating excellent calibration.

B Physically-Informed Pixel Confidence M_i Details

we generate a domain expert-informed probability of the label correctness for each surface water pixel i :

$$p_{\text{final}} = \alpha_1 \cdot p_{\text{dischargers}} + \alpha_2 \cdot p_{\text{landcover}} + \alpha_3 \cdot p_{\text{sample_dist}} + \alpha_4 \cdot p_{\text{downstream}} \quad (5)$$

where $p_{\text{dischargers}}$, $p_{\text{landcover}}$, $p_{\text{sample_dist}}$, and $p_{\text{downstream}}$ represent probabilities derived from (i) proximity to PFAS dischargers, (ii) land cover type, (iii) distance to other sample points, and (iv) downstream flow, respectively. In detail:

- **Proximity to PFAS Dischargers ($p_{\text{dischargers}}$)** Proximity to known PFAS dischargers is a strong indicator of contamination risk, as shown in scientific analyses³. If a pixel’s label is 1, we apply an exponential decay function of distance, assigning higher probabilities to pixels closer to known dischargers. For pixels labeled 0, we invert this logic so that being near a discharger lowers confidence in the 0 label.
- **Land Cover Type ($p_{\text{landcover}}$)** For pixels labeled 1, surrounding urban or built-up areas received higher probabilities, consistent with research linking PFAS to industrial zones⁴. Conversely, for 0-labeled pixels, surrounding undeveloped or forested land cover increased confidence in low contamination.
- **Proximity to Other Sample Points ($p_{\text{sample_dist}}$)** Pixels closer to ground truth sample points were assigned higher probabilities using an exponential decay function based on distance to each sample point in the raster.
- **Downstream Flow ($p_{\text{downstream}}$)** PFAS may also travel downstream in aquatic systems, making hydrologic flow another critical factor in contamination spread⁵. If a pixel lies downstream of a sample point labeled 1, its probability for label 1 increases, and similarly for label 0. This flow direction channel was generated using ArcGIS Pro⁶ based on digital elevation models (DEMs)⁷.

Full performance results for all configurations are reported in Table 8, demonstrating that our selected weighting scheme most effectively balances the different environmental signals for robust PFAS contamination prediction.

³PFAS dischargers

⁴Landcover

⁵Downstream Flow

⁶ArcGIS Pro

⁷DEM

Table 8: Performance across all noise mask weight configurations using the 2008 PFAS dataset.

Dischargers (%)	Landcover (%)	Flow Dir. (%)	Sample Dist. (%)	IoU (%)	F-score (%)	Precision (%)	Recall (%)	Accuracy (%)
40	20	30	10	48	61	61	64	73
40	30	20	10	44	55	58	52	70
40	10	30	20	46	59	60	56	72
40	10	20	30	42	53	55	51	69
40	30	10	20	45	57	59	54	71
40	20	10	30	43	54	57	52	70
30	40	10	20	46	58	60	55	72
30	40	20	10	43	56	57	53	68
30	10	40	20	44	55	56	53	69
30	10	20	40	45	57	58	55	70
30	20	40	40	47	62	60	58	72
30	20	10	40	45	58	59	56	71
30	10	30	30	41	52	54	49	69
10	40	30	20	47	60	60	58	72
10	40	20	40	44	56	57	54	69
10	30	40	20	42	53	55	51	70
10	30	20	40	43	55	56	52	68
10	20	40	10	46	59	60	57	72
10	20	30	40	44	56	57	53	70
20	40	30	40	45	58	59	56	69
20	40	10	30	46	59	60	57	72
20	30	40	10	44	57	58	55	69
20	30	20	30	43	56	57	54	68
20	10	40	30	40	52	54	50	66

C Kriging

We employed Kriging as a spatial interpolation technique to estimate PFAS. First, we examined the spatial structure of our data by calculating an empirical semivariogram. Using latitude and longitude coordinates alongside the binary target variable, we computed pairwise distances and differences to produce a semivariogram plot, enabling us to observe how variance changed with increasing distance. This step informed the selection of appropriate variogram models (e.g., linear or spherical) for Kriging. Based on this analysis, we selected a spherical variogram model, which best captured the spatial dependencies observed in our data.

Next, we split the data on a state-by-state basis, ensuring geographic diversity between the training and testing subsets. We explored both Ordinary Kriging (assuming a stationary mean across the study area) and Universal Kriging (introducing a drift term to account for regional linear trends), but the two approaches produced comparable results on our dataset. After training each Kriging model on the geographic regions in the training set, we predicted PFAS presence at test set locations. Since we treated PFAS presence as a binary outcome, the resulting continuous Kriging predictions were thresholded at 0.5. We then computed standard classification metrics (such as precision, recall, and F1-score) to evaluate each model’s ability to distinguish between high contamination versus low contamination sites.

While Kriging provided a practical means of interpolating PFAS presence, its reliance on variogram assumptions and spatial stationarity can limit accuracy in areas with highly heterogeneous conditions.

D Pollutant Transport Simulation

Instead of running a simulation like SWAT directly, which is designed for general watershed hydrology modeling but lacks established parameterization for PFAS transport, we implemented a streamlined Python-based workflow more tailored to PFAS-related surface water contamination. This approach allowed us to integrate domain-relevant features without relying on assumptions unsupported by current PFAS science.

First, we assign initial pollutant concentrations in each patch by setting cells flagged as “dischargers” to a high baseline value (e.g., 100), while land cover–based default concentrations provide moderately-low to low initial contamination levels for other cells. We then construct a Hydrologic Response Unit (HRU) parameter table

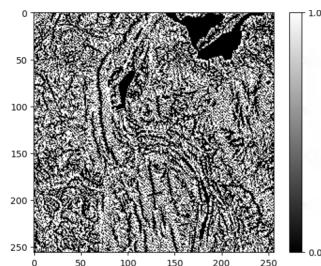


Figure 10: Example binary output from the pollutant transport simulation: 0 represents low contamination, and 1 represents high contamination. The simulation approximates the distribution of PFAS contamination based on hydrological and environmental parameters, providing a practical alternative to full-scale SWAT simulations.

that assigns infiltration and runoff values based on a cell’s land cover, soil type, and slope. Using these parameters, each patch’s land cover and soil rasters define infiltration/runoff ratios for every grid cell. We incorporate two key rasters; flow direction and flow accumulation, both exported from System for Automated Geoscientific Analyses (SAGA); a GIS and geospatial analysis tool focused on geospatial data processing, analysis, and visualization, to specify how water and pollutant mass move downstream. In each iteration, a fraction of the pollutant mass in each cell is transferred to its downstream neighbor according to the cell’s infiltration/runoff factors, guided by the flow direction raster and scaled by the flow accumulation values. Repeating this process causes pollutant mass to concentrate in lower-lying or higher-flow cells, thereby modeling how contamination evolves over time within the patch.

After the simulation converges, we produce a final pollutant concentration raster, thresholded by the median value of concentrations across all patches for the year to generate a binary contamination map, as illustrated in Fig. 10. The binary outputs, with values of 0 and 1 representing low and high contamination respectively, visualizes the simulation’s predictions of contamination distribution. These outputs are compared against test set patches containing actual observed PFAS presence *in surface water* to evaluate how accurately the simulation captures observed contamination patterns. Although this standalone approach remains computationally non-trivial, it is more tractable for batch processing of multiple patches than running a full SWAT project repeatedly. Consequently, it provides a practical baseline for pollutant transport modeling within our broader framework, allowing us to compare simulated outputs to both real-world data and other modeling approaches.

E Consistency Analysis

To evaluate local spatial consistency, we applied a robustness test across all 49 continental U.S. states. For each state, we extracted two overlapping image patches; one with a 56×56 pixel overlap and another with 156×156, using three different random locations to ensure stability. We then compared the model’s predictions over the overlapping regions by computing pixel-wise agreement. Agreement is the proportion of matching predicted labels across overlapping pixels between two patches:

$$\text{Agreement} = \frac{1}{N} \sum_{i=1}^N \mathbf{1}(y_i^{(1)} = y_i^{(2)}), \quad (6)$$

where $y_i^{(1)}$ and $y_i^{(2)}$ are the predicted labels for the i^{th} pixel in each patch, and N is the total number of overlapping pixels.

Table 9 reports the agreement across different years using our final FOCUS model. The high consistency scores across both overlap sizes demonstrate that the model generates stable predictions for the same spatial region even when seen in different contexts. This supports the reliability of our framework in real-world geospatial settings.

Table 9: Spatial consistency measured as prediction agreement over overlapping patch regions.

Year	56x56 Overlap	156x156 Overlap
2008	95 ± 1 %	93 ± 1 %
2019	96 ± 2 %	98 ± 2 %
2022	93 ± 1 %	94 ± 1 %

F Evaluating the Impact of Noise Masks on Segmentation of Land Cover Types

In this experiment, as introduced in Section 3.3, we FOCUS on distinguishing between two pairs of land cover (LC) types:

- **Evergreen Forests vs Barren Land** (Class 0: Barren Land, Class 1: Evergreen Forest)
- **Deciduous Forests vs Water** (Class 0: Deciduous Forest, Class 1: Water)

In this experiment, we simulate uncertainty in the labeling process to align with the uncertainty potentially present in our PFAS ground truth label expansion. Specifically, we randomly throw out half of the valid class pixels and replace them with the other class’s label. We then generate noise masks using only the NDVI values, which are used during the training process to handle the uncertainty.

Results Below are the macro-averaged results showing the performance metrics for the Evergreen Forests vs Barren Land and Deciduous Forests vs Water pairs, both with and without noise masks. These LC image patches are aligned with the same spatial footprint as the PFAS patches to ensure consistency in coverage. The evaluation is conducted on at most 2 pixels per image patch, simulating sparse ground truth availability similar to the PFAS setting. We see that including noise masks is useful in this setting as well.

Table 10: Performance Comparison for Evergreen Forests vs Barren Land: Simulated Uncertainty in PFAS Pseudolabeling

Evergreen Forests vs Barren Land		Performance Metrics			
Method	IoU	F1-Score	Precision	Recall	Accuracy
With Noise Masks	0.38	0.55	0.56	0.56	0.55
Without Noise Masks	0.24	0.33	0.74	0.50	0.48

Table 11: Performance Comparison for Deciduous Forests vs Water: Simulated Uncertainty in PFAS Pseudolabeling

Deciduous Forests vs Water		Performance Metrics			
Method	IoU	F1-Score	Precision	Recall	Accuracy
With Noise Masks	0.38	0.55	0.55	0.56	0.55
Without Noise Masks	0.33	0.49	0.51	0.51	0.52

G Dataset

The dataset was curated to ensure that patches included in the training and testing sets were geographically disjoint, avoiding any overlap.

In cases where two or more patches overlapped, as illustrated in Fig. 11, all such patches were assigned to the same set (either training or testing). This ensured that no part of a test patch had been seen during training, preserving the integrity of the evaluation.



Figure 11: Example of overlapping patch assignment. The figure illustrates two slightly overlapping patches overlaid on the U.S. map, each containing distinct sample points. To maintain disjoint training and testing sets, both patches are assigned to the same set (either training or testing), ensuring no part of a test patch overlaps with any patch seen during training.

Additionally, Table 12 expands on the table in Section 3.5.1 to include class distribution. There is a significant class imbalance that we observe in the real world: unfortunately, a majority of water bodies have PFAS contamination that exceed health guidelines, as found in prior scientific work on PFAS prediction as well ⁸. To affirm that there is in fact signal to our predictions, we provide class-specific results in Section H. For instance, we find approximately 80% F-score for class 0 for the year 2024, showing we are truly predicting class 0, and better than random. We also add a ternary classification in Section I to provide additional levels of risk.

Table 12: Datasets used for training, testing, and real-world validation, including total size and class balance.

Type	Use	Data Source	Total Size	% Pos / Neg
Fish	Train/Test	EPA [58, 59]	866	89.5% / 10.5%
Fish	Validation	MPART [35]	114	77.2% / 22.8%
Water	Train/Test	MPART [34]	293	66.9% / 33.1%
Water	Real-World Validation	Sampled by Authors	8	100% / 0%

⁸See: *PFAS pollute 83% of U.S. waterways*, E&E News by Politico (2023). Available at: <https://www.eenews.net/articles/pfas-pollute-83-of-u-s-waterways/>

H FOCUS Per-Class Results

To better understand model behavior across classes, Table 13 reports per-class performance metrics for FOCUS across each year, including results on the 2024 MPART surface water dataset.

Table 13: Per-class performance of our model using FOCUS across four years (MPART surface water results at 2024). Results averaged over 3 random seeds.

Metric	2008 (%)		2019 (%)		2022 (%)		2024 (%)	
	Class 0	Class 1						
Accuracy	73 ± 1	73 ± 1	82 ± 1	82 ± 1	88 ± 2	88 ± 2	79 ± 2	79 ± 1
IoU	25 ± 2	70 ± 2	40 ± 2	79 ± 2	47 ± 3	87 ± 2	67 ± 2	63 ± 2
F-score	40 ± 2	82 ± 2	57 ± 2	88 ± 2	64 ± 3	93 ± 2	80 ± 2	77 ± 2
Precision	33 ± 3	88 ± 2	42 ± 2	98 ± 2	60 ± 3	94 ± 1	75 ± 1	83 ± 2
Recall	50 ± 2	78 ± 2	89 ± 1	80 ± 1	69 ± 1	92 ± 2	86 ± 1	71 ± 1

I Ternary Classification of Hazard Levels

To enable finer-grained prioritization of contamination severity, we extended our binary classification framework to a ternary setting. Specifically, each fish tissue sample was assigned to one of three classes based on its hazard index (HI), defined as the ratio of measured PFAS concentration to the EPA’s reference dose:

- **Class 0 (Low):** $HI < 1$ (i.e., below the EPA baseline threshold)
- **Class 1 (Medium):** $1 \leq HI \leq 1000$
- **Class 2 (High):** $HI > 1000$

The threshold of 1000 was informed by a combination of data-driven distributional patterns and recent regulatory guidance. In particular, the updated 2025 Michigan Department of Health and Human Services fish consumption guidelines define a 50 ppb (do-not-eat) threshold; approximately a 900× range relative to the EPA’s 0.056 ppb PFOS reference dose. While these thresholds may vary by state, the Michigan values are among the most recent and provide a concrete, health-based rationale for distinguishing especially high-risk cases. It also corresponds well with natural breakpoints observed in our hazard index distributions.

Table 14: Performance of FOCUS under ternary classification (0: low, 1: medium, 2: high). Results averaged over 3 random seeds.

Metric	2008 (%)	2019 (%)	2022 (%)
Accuracy	55 ± 1	72 ± 1	65 ± 1
IoU	38 ± 1	48 ± 2	44 ± 2
F-score	54 ± 1	63 ± 1	61 ± 1
Precision	66 ± 2	70 ± 2	60 ± 2
Recall	65 ± 2	61 ± 1	62 ± 2

Results demonstrate signal, but are less strong compared to FOCUS binary classification performance, given the added complexity of the ternary task.

J Statistical Significance of Performance Gains

To evaluate the robustness of our improvements over the focal-only baseline, we conducted statistical significance testing using the Wilcoxon signed-rank test, a non-parametric paired test appropriate for comparing performance across random seeds.

For each year (2008, 2019, 2022), we collected the F-scores from multiple runs (5 seeds per year) and compared the FOCUS results against focal-only using a two-sided Wilcoxon signed-rank test. As shown in Table 15, FOCUS achieved statistically significant improvements in all three years ($p = 0.03125$), despite the relatively small number of seeds. Notably, for every random seed, the F-score achieved with FOCUS was consistently higher than the focal-only counterpart.

These results confirm that the performance gains from our noise-aware loss are not due to chance, but are statistically reliable across different random initializations.

Table 15: Wilcoxon signed-rank test comparing F1-scores of FOCUS and focal-only across 5 random seeds for each year.

Year	Wilcoxon Statistic	p -value
2008	0.0	0.03125
2019	0.0	0.03125
2022	0.0	0.03125

K Distance-to-Industry Rasters

To capture potential industrial sources of PFAS contamination, we constructed distance rasters for each relevant facility type using data from the EPA’s ECHO database. For each year (e.g., 2008, 2019, 2022), we identified all facilities that were active *on or before* that year, ensuring historical context was preserved. Facility types were grouped by industrial category (e.g., airports, landfills, chemical manufacturers), and a separate Euclidean distance raster was generated for each category, where pixel values represent the distance to the nearest facility of that type.

The total number of distance raster channels therefore varies by year, depending on which facility types were present in the ECHO dataset up to that point. For example, a given year may include distance rasters for 15 industry types, while another may include 41.

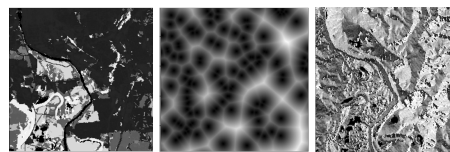


Figure 12: Example raster channels in an image: (left) land cover, (center) distances from chemical manufacturing industries, and (right) flow direction.

L Ablation Results for Image Resolution

Table 16 presents the results of our image resolution ablation study. We compare the model’s performance when trained on 256×256

versus 512×512 input resolutions, without the use of noise-aware training.

Table 16: Comparison of performance between 256×256 and 512×512 image resolutions without noise-aware training. Bold values indicate the better result.

Metric	2008 (%)		2019 (%)		2022 (%)	
	256	512	256	512	256	512
Accuracy	37 ± 2	35 ± 3	62 ± 1	59 ± 2	55 ± 3	49 ± 3
IoU	22 ± 3	20 ± 2	41 ± 2	40 ± 2	36 ± 3	32 ± 2
F-score	36 ± 3	32 ± 3	57 ± 1	54 ± 2	53 ± 3	50 ± 3
Precision	54 ± 2	50 ± 3	63 ± 2	57 ± 2	63 ± 3	61 ± 3
Recall	55 ± 2	51 ± 2	78 ± 1	70 ± 2	74 ± 1	70 ± 2

M Hyperparameter Tuning and Selection

We tuned the learning rate and batch size empirically by monitoring training stability. Specifically, we experimented with learning rates in $\{1 \times 10^{-3}, 5 \times 10^{-4}, 1 \times 10^{-4}\}$ and batch sizes in $\{2, 4, 8\}$. We selected a batch size of 4 because it provided the best stability while preserving the benefits of our pretrained backbone, minimizing the risk of large, destabilizing updates. Notably, these final hyperparameter values are consistent with those adopted in the original Prithvi paper, further supporting their suitability in this context.

N Technical Details on Sample Analysis and Training Data for Real-World Predictions

This section provides additional technical details on the real-world PFAS samples collected and analyzed by our team.

Sample Collection. New 250 mL HDPE (High-Density Polyethylene) bottles were triple rinsed with ultrapure water before sample collection in the field.

Sample Preparation. Samples were extracted using solid phase extraction, guided by EPA Method 1633. Each sample was spiked with 200 μ L of isotopically mass-labeled standards (Wellington).

Targeted Sample Analysis. Targeted PFAS analysis was conducted using a Thermo Exploris 240 Orbitrap mass spectrometer (MS) coupled with a Vanquish ultra-high-performance liquid chromatograph (UHPLC-MS). A C-18 column was used, and the MS was operated in negative electrospray ionization (ESI-) mode.

Model Used for Prediction. The model used to generate predictions for these newly collected samples was trained on 2024 surface water samples from the Michigan MPART dataset. Given the temporal proximity and coverage of this dataset, it provided a decent foundation for making informed predictions on samples collected in mid-2025.

O FOCUS Loss Derivation and Assumptions

Setup (latent asymmetric flip noise). Let $z_i \in \{0, 1\}$ be a latent clean label and $y_i \in \{0, 1\}$ the observed noisy label. Assume per-pixel flip noise with rate $\eta_i \in [0, \frac{1}{2}]$ (can be asymmetric and spatially

varying):

$$\Pr(y_i = z_i | x_i) = 1 - \eta_i, \quad \Pr(y_i \neq z_i | x_i) = \eta_i.$$

Let $\pi_\theta(x_i) = \Pr_\theta(z_i = 1 | x_i)$ and define $\pi_\theta^{(y_i)}(x_i) = \pi_\theta(x_i)$ if $y_i = 1$ and $1 - \pi_\theta(x_i)$ if $y_i = 0$. Then the noisy likelihood is

$$\Pr(y_i | x_i) = \eta_i + (1 - 2\eta_i) \pi_\theta^{(y_i)}(x_i), \quad (7)$$

and the per-example noisy negative log-likelihood (NLL) is

$$\ell_{\text{noisy}}(\theta; x_i, y_i) = -\log\left(\eta_i + (1 - 2\eta_i) \pi_\theta^{(y_i)}(x_i)\right). \quad (8)$$

Lemma O.1 (Local weighted-CE upper bound). *Fix $\eta_i \in [0, \frac{1}{2}]$ and an anchor $p_{0i} \in (0, 1)$. Let $g_i(p) = -\log(\eta_i + (1 - 2\eta_i)p)$. Then for all p in a neighborhood of p_{0i} ,*

$$g_i(p) \leq g_i(p_{0i}) + g'_i(p_{0i})(p - p_{0i}) = -w_i \log p + C_i, \quad (9)$$

where

$$w_i = \frac{(1 - 2\eta_i)p_{0i}}{\eta_i + (1 - 2\eta_i)p_{0i}} \in [0, 1], \quad C_i = g_i(p_{0i}) + w_i \log p_{0i}. \quad (10)$$

Interpretation. Lemma O.1 implies the noisy NLL behaves locally like a *weighted cross-entropy* term $-w_i \log p$, and the weight w_i decreases as η_i increases (labels become less informative).

Assumption on M_i (role of the environmental priors-informed confidence). We use $M_i \in [0, 1]$ as a practical surrogate for the unknown reliability weight. Concretely, we assume M_i is *aligned with label cleanliness: (Alignment assumption)*. We assume that $\mathbb{E}[M_i | \eta_i]$ is non-increasing in η_i , and that M_i approximates w_i up to a monotone re-scaling:

$$\mathbb{E}[M_i | \eta_i] \downarrow \text{ in } \eta_i, \quad M_i \approx w_i. \quad (11)$$

Intuitively, M_i is larger near locations where supervision is more trustworthy (e.g., near sampling points or along plausible hydrologic pathways) and smaller in regions where point-to-pixel propagation is likely wrong.

We next show that multiplying by a bounded focal factor preserves a local surrogate form.

Lemma O.2 (Focal modulation preserves local surrogate form). *Fix $\gamma \geq 0$ and anchor $p_{0i} \in (0, 1)$. There exist constants $A_i > 0$ and B_i such that for all p near p_{0i} ,*

$$-\log(\eta_i + (1 - 2\eta_i)p) \leq A_i (1 - p)^\gamma (-\log p) + B_i. \quad (12)$$

Interpretation. Near a fixed operating point p_{0i} , $(1 - p)^\gamma$ is a positive bounded scalar, so focal loss is a locally rescaled cross-entropy and retains classification-calibrated behavior.

We now connect the above lemmas to the proposed objective.

Theorem O.3 (FOCUS as a noisy-NLL surrogate (local)). *Under the model in (7)–(8) and $\gamma \geq 0$, for each example i there exist constants $\tilde{A}_i > 0, \tilde{B}_i$ such that for all p near p_{0i} ,*

$$\ell_{\text{noisy}}(\theta; x_i, y_i) \leq \tilde{A}_i M_i (1 - p)^\gamma (-\log p) + \tilde{B}_i, \quad \text{where } p = \pi_\theta^{(y_i)}(x_i).$$

Equivalently, minimizing

$$\mathcal{L}_{\text{FOCUS}}(x_i, y_i) = M_i (1 - \pi_\theta^{(y_i)}(x_i))^\gamma (-\log \pi_\theta^{(y_i)}(x_i)) \quad (13)$$

minimizes a valid local upper bound on ℓ_{noisy} (up to constants), and thus maximizes a corresponding local lower bound on the noisy log-likelihood.

Connection to expected noisy risk and calibration. Aggregating Theorem O.3 over pixels yields a surrogate for the expected noisy risk $\mathbb{E}[\ell_{\text{noisy}}]$. Since the modulating factor is non-negative and bounded for $p \in (0, 1)$ and $\gamma \geq 0$, the objective remains classification-calibrated in the standard sense (locally equivalent to CE).

Edge cases and sanity checks.

- **Clean-label limit.** If $\eta_i \rightarrow 0$, then $w_i \rightarrow 1$ in (10). If additionally $M_i \rightarrow 1$, then FOCUS reduces to standard focal loss; with $\gamma = 0$ it reduces to CE.
- **Uninformative-label limit.** If $\eta_i \rightarrow \frac{1}{2}$, then $w_i \rightarrow 0$. Under the alignment assumption (11), M_i also becomes small, so FOCUS naturally down-weights (or effectively ignores) pixels whose supervision is uninformative.
- **Calibration of M_i .** In practice M_i need not equal the true w_i ; it suffices that M_i ranks pixels by reliability (monotone alignment). This is precisely the role of our environmental priors-informed construction.

P Region-Level Risk Signals and Bioaccumulation Evidence

To assess the scientific relevance of model predictions beyond pixel-level accuracy, we aggregate surface-water contamination predictions into region-level risk categories and examine their spatial correspondence with independent fish advisory evidence [36] over Michigan (Fig 13). Predicted surface-water contamination categories show spatial agreement with regions exhibiting elevated fish contamination, supporting a link between modeled water contamination risk and bioaccumulation-related risk signals.

At the same time, discrepancies between predicted high-risk waters and advisories highlight regions for targeted sampling and scientific follow-up. This analysis illustrates how noise-aware geospatial learning supports AI for Science by integrating large-scale data with sparse observations to guide future measurement efforts.

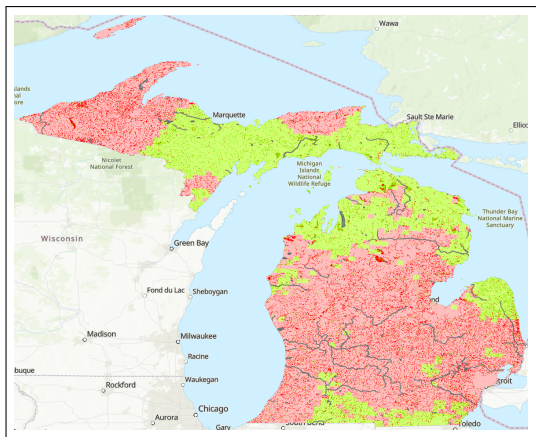


Figure 13: Region-level aggregation of predicted surface-water PFAS risk over Michigan. Colors indicate low (green), and high (red) predicted risk. Overlaid regions (polylines) correspond to independent fish consumption advisory areas from state monitoring programs.